Microchimica Acta (2022) 189:391
https://doi.org/10.1007/s00604-022-05482-4

ORIGINAL PAPER

Conductive metal–organic framework based label-free electrochemical detection of circulating tumor DNA

Juan Liu[1] · Siyi Yang[1] · Jinhui Shen[1] · Huanbao Fa[2] · Changjun Hou[1,3] · Mei Yang[1,3]

Received: 25 April 2022 / Accepted: 29 August 2022 / Published online: 23 September 2022

Abstract

An ultrasensitive electrochemical biosensor was designed for the rapid label-free detection of circulating tumor DNA (ctDNA, EGFR 19 Dels for non-small cell lung cancer, NSCLC). We linked the highly conjugated tricatecholate, 2,3,6,7,10,11-hexahydroxytriphenylene (HHTP) with Ni(II) ions into the two-dimensional porous conductive metal–organic frameworks (MOFs), which is termed Ni-catecholates (Ni-CAT). Then, the AuNPs/Ni-catecholates/carbon black/polarized pencil graphite electrode (AuNPs/Ni-CAT/CB/PPGE) was obtained by electrodeposition of AuNPs on the surface of PPGE modified with Ni-CAT/CB composite materials. The AuNPs/Ni-CAT/CB/PPGE were used for label-less detection of ctDNA, with a total detection time of only 30 min. Under optimal detection conditions, the AuNPs/Ni-CAT/CB/PPGE sensor exhibited excellent detection performance with good linear response to ctDNA over a wide concentration range and the detection limit down to the femtomolar level. The sensor was applied to the determination of ctDNA in serum samples with high sensitivity. This simple, efficient, and expeditious method has practical value in liquid biopsy of ctDNA and has potential for development in early detection, treatment, and prognosis of tumors.

Keywords ctDNA · Conductive MOFs · Label-free · Electrochemical sensor · Differential pulse voltammetry

Introduction

As a tumor biomarker, ctDNA testing has indubitable high potential in the early diagnosis, prognostic monitoring, and detection of drug resistance in tumors. The challenges in detecting ctDNA are the low levels, the short half-life, and the high degree of fragmentation [1, 2]. Recently, multiple techniques have been used to qualitative detection of ctDNA in liquid biopsies [3, 4]. For example, droplet digital PCR (ddPCR), bead, emulsion, amplification, and magnetic (BEAMing), amplification refractory mutation system (ARMS), and next-generation sequencing technology (NGS). All of the above analysis strategies have high sensitivity and can detect ctDNA accurately, while the drawbacks of them are large instrument requirement and analysis time-consuming. Meanwhile, in the recent years, biosensors are gaining attention as an alternative of traditional analytical methods in the detection of biomolecules because of their high incomparable specificity, sensitivity, and simplicity. Several biosensing strategies have been applied to the detection of ctDNA [5, 6]. For instance, a novel sensitive dual-recognition fluorescent device, a visible strategy based on ctDNA-triggered and DNAzyme-functionalized hydrogel, hybridization chain reaction (HCR)-assisted amplification nanopore biosensors, surface-enhanced Raman scattering (SERS) strategy for enzymatic amplification. However, the detection limits achieved by these detection strategies are mostly at the unsatisfactory results, which failed to meet the requirements in ctDNA detection. And the tests often take several hours, which do not meet the need for speed and efficiency in ctDNA assays.

✉ Changjun Hou
houcj@cqu.edu.cn

✉ Mei Yang
yangmei@cqu.edu.cn

[1] Key Laboratory of Biorheological Science and Technology, Ministry of Education, College of Bioengineering, Chongqing University, Chongqing 400044, People's Republic of China

[2] College of Chemistry and Chemical Engineering, Chongqing University, Chongqing 400044, People's Republic of China

[3] College of Bioengineering, Chongqing University, Chongqing 400044, People's Republic of China

Furthermore, among the numerous bio-sensing detection methods, electrochemistry has high potential for application due to numerous advantages such as low-cost high sensitivity, and excellent specificity, and can be combined with other strategies to improve test results. On the one hand, combining electrochemical sensors with signal amplification strategies is also a common approach to achieve higher detection capacity and improved selectivity for ctDNA analysis. For instance, rolling circle amplification (RCA) [7], DNA Walkers [8] and hybridization chain reaction (HCR) are all proven amplification techniques that can be used separately or simultaneously [9]. However, these co-amplification techniques are tended to be time-consuming and more likely to cause experimental errors during cumbersome procedures. Therefore, the strategies with simple and convenient operation attract much more attention, which has the advantages of low detection cost, fast response, and label-free process. On the other hand, it helps to improve electrochemical sensor performance by investigating novel nanomaterials as sensing interface [10, 11], such as urchin-like Au/multiple graphene aerogel, three-dimensional (3D) porous nitrogen-doped graphite carbon composites functionalized with Fe3C (Fe3C/NG), 2D siloxene sheets, single-atom Co(II) coordinated on an N-doped graphene matrix (A–Co–NG). Processing electrodes through materials is a relatively simple and effective strategy for sensor performance enhancement.

MOF material, a new porous material with high specific surface area, controllable pores and variable structure, has been widely used in electrochemical sensing. For example, Ni-MOF-74, NH_2-MIL-101(Fe), PCN-222, and other MOFs have been applied to electrochemical detection methods for different targets [12, 13]. However, MOF materials typically have poor electrical conductivity and stability, which hinder their electrochemical applications. Recently, researchers have been drawn to a novel type of conductive MOF material with high electrical conductivity. The conductive MOFs composed of benzene or triphenylene-derived ligands with a variety of transition metals can greatly enhance electrical conductivity and aid in electron transport due to the highly conjugated and off-domain π bonds in the ligands [14]. Meanwhile, the conductive MOFs have one-dimensional cylindrical channels to facilitate ion transport and achieve high ionic conductivity [15]. Due to this property, these materials have a wide range of applications in electrochemistry, especially in supercapacitors, batteries, etc. [16]. In recent years, it has also been gradually used for research in the field of sensing. Xu [17] in situ growth of Ni/Co (HHTP) MOF on carbon cloth (CC) for the direct detection of glucose. The Ni/Co (HHTP) MOF/CC sensor provides more catalytic active sites and larger surface area. The detection limit is 100 nM (S/N = 3) and the response time is 2 s. Ko [18] used various conductive MOF (M_3HXTP_2; M = Ni, Cu; and X = NH, 2,3,6,7,10,11-hexaiminotriphenylene (HITP) or O, 2,3,6,7,10,11-hexahy droxytriphenylene (HHTP)) modified glassy carbon electrodes (GCE) for the voltammetric determination of neurochemicals such as ascorbic acid (AA), dopamine (DA), uric acid (UA), and serotonin (5-HT). The results revealed that Ni-catecholates (Ni-CAT) can achieve nanomolar detection limits for DA and 5-HT with a wide detection range. However, the novel kind of conductive MOFs is seldom applied to the teleological detection of large molecules such as proteins and nucleic acids up to now.

In this work, the conductive Ni-CAT is innovatively applied to prepare ctDNA electrochemical biosensor for nucleic acid detection (Scheme 1). We obtained 2D conductive Ni-CAT by a simple and convenient one-step hydrothermal synthesis with nickel salt and triphenylene-2,3,6,7,10,11-hexaol (HHTP). And carbon black (CB), as an inexpensive and readily available carbon material [19], can be embedded in the gaps of the unevenly arranged stick-like Ni-CAT, which helps to enhance the conductivity and stability of the electrode. Finally, AuNPs are deposited on the electrode surface to provide attachment sites for probe DNA (pDNA). After ligation of the pDNA, the binding site is closed with MCH to prevent non-specific adsorption. The recognition of the target by base complementary pairing with the pDNA has an effect on electron transfer at the electrode, leading to a reduction in current, as can be observed in the decrease in peak differential pulse voltammetry (DPV) current. This label-free detection strategy effectively addresses the problem of time-consuming bio-amplification, while being simple and cost effective to operate. In our study, the pDNA/AuNPs/Ni-CAT/CB/PPGE label-free electrochemical biosensor was successfully prepared with high sensitivity, broad detection range, low detection limit, and short detection time.

Experimental section

Materials and reagents

Phosphate buffer solution (PBS), triphenylene-2,3,6,7,10,11-hexaol (HHTP) were purchased from Ademas-beta Co., Ltd (Shanghai, China). Polyvinyl alcohol (PVA), nickel acetic acid tetrahydrate ($Ni(CH_3COO)_2{\cdot}4H_2O$), hydrogen tetrachloroaurate trihydrate ($HAuCl_4{\cdot}4H_2O$), and phosphine hydrochloride (TCEP) were purchased from Aladdin Co., Ltd (Shanghai, China). The 6-mercaptohexan-1-ol (MCH) was purchased from Sigma-Aldrich (St. Louis, USA). Normal human serum was purchased from Solarbio Tech. Co., Ltd. (Beijing, China). Carbon black (CB) is purchased from Xinxiang Delong Chemical Co., Ltd. (Henan China). All Synthetic DNA oligonucleotide sequences were provided by Sangon Biotech Co., Ltd (Shanghai, China). The sequences of oligonucleotides are listed in Table 1. All other chemicals

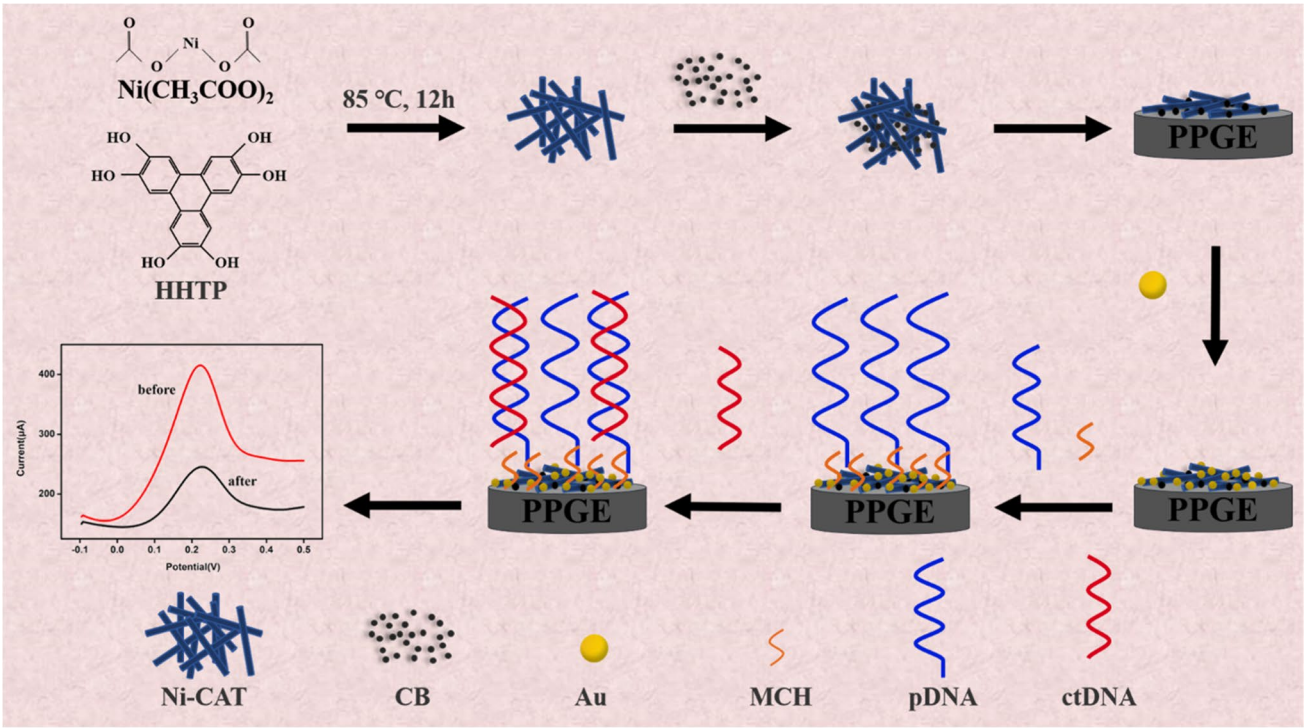

Scheme 1 Schematic illustration of the AuNPs/Ni-CAT/CB/PPGE biosensor

Table 1 The base sequences of oligonucleotides used in the work

DNA oligonucleotides sequences	5′→3′
Target ctDNA (EGFR 19 del (1))	GTC GCT ATC AAA ACA TCT CCG AAA G
Interfering DNA (EGFR 19 del (2))	GTC GCT ATC AAG ACA TCT CCG AAA G
Wild type	CTA TCA AGG AAT TAA GAG AAG CAA C
probe DNA (pDNA)	SH-$(CH_2)_6$-AAA CTT TCG GAG ATG TTT TGA TAG CGA CAA A

were of analytical-reagent grade and used without further purification, and all aqueous solutions were freshly prepared with deionized water (DI) (18.2 MΩ·cm) with a Milli-Q Water system.

Apparatus

The morphology of nanomaterials is jointly characterized by field-emission scanning electron microscopy (FE-SEM, FEI Nova 400) and energy dispersive spectroscopy (EDS, JEOL-6300F). X-ray diffraction (XRD) patterns were recorded using a Bruker AXS D5005 (Bruker, Germany). X-ray photoelectron spectroscopy (XPS) measurements were conducted using a 5300 ESCA instrument (PerkinElmer PHI Co., USA). Cyclic voltammetry (CV), differential pulse voltammetry (DPV), and other electrochemical measurements were performed on a CHI760E electrochemical workstation (Shanghai Chenhua Instruments Co. Ltd, China). The three-electrode system was employed in the detection system; an Ag/AgCl (3 M KCl) was used as reference electrode; a platinum wire electrode was used as the counter electrode; and polarized pencil graphite electrode (PPGE) was used as work electrode.

Preparation of Ni-CAT and Ni-CAT/CB nanocomposites

Ni-CAT was synthesized in a single step, as previously reported [20]. In a glass vial, the mixture of HHTP (7 mg) and $Ni(CH_3COO)_2{\cdot}4H_2O$ (10 mg) was dissolved in deionized water (4.0 mL). The reaction mixture was baked at 85 °C for 12 h to produce a dark blue solid with inky blue

supernatants. The reaction mixture was allowed to cool naturally to ambient temperature before being centrifuged at 10,000 rpm for 10 min to obtain a solid precipitate, which was then washed with deionized water for 3 times and acetone for 6 times. The obtaining crystals are dried at room temperature under a vacuum and stored at 4 °C for further use.

Before the preparation of Ni-CAT/CB nanocomplexes, pretreatment of CB is required. PVA (20 mg) was added into deionized water (10 mL), stirring for 30 min. Then CB (40 mg) was joined and stirring for another 24 h to obtain a well-dispersed aqueous solution of CB (2 mg/mL). Meanwhile, Ni-CAT was prepared into aqueous solution with the same concentration of CB solution. During the experiment, the two solutions were mixed in different proportions (the ratio of Ni-CAT to CB is 3:1, 2:1, 1:1, 1:2, 1:3). The two solutions are mixed by oscillation and ultrasonic to obtain Ni-CAT/CB nanocomplexes.

Fabrication of biosensing platform

Firstly, we wrapped a 2-mm-diameter HB pencil lead with Teflon tape and exposed the surface of the electrode about 1 mm, then polished the surface with sandpaper (1000 grit) and wet cloth. The electrodes mentioned above were immersed in 10 mL of 0.1 M PBS (pH 7.0) and pretreated by cyclic voltammetry (CV) (scanning potential of 1.5 ~ 2 V, sweeping speed of 0.05 V/s, scanning 50 cycles) [21]. After scanning, we rinsed the electrode several times with deionized water to gain a PPGE, drying at room temperature, and set aside.

Secondly, the prepared Ni-CAT/CB composite solution (5 μL) was dripped onto the PPGE surface, and let it dry at ambient temperature. After that, Ni-CAT/CB/PPGE electrodes were immersed in 10 mL of 2 mM $HAuCl_4$ solution and deposited a layer of gold nanoparticles on the surface of the electrode by chronoamperometry (i-t); the specific parameters were an initial potential of − 0.2 V and duration time of 120 s. After scanning, the electrodes were washed with deionized water a few times and dried at room temperature. AuNPs/Ni-CAT/CB/PPGEs were successfully prepared for subsequent experiments.

Then, the linear annealed pDNA solution (10^{-9} M) was mixed with an equi-volume of TCEP solution (1 mM), and reacted for 1 h at room temperature to activate the –SH moiety. Five microliters of the mixed solution was dropped to the AuNPs/Ni-CAT/CB/PPGE surface and incubated for 2 h at 37 °C before being washed with PBS solution (pH = 7.4) to remove unbound pDNA. Finally, 5 μL of the MCH solution (1 mM) was applied on the electrode surface and reacted for 1 h to block the uncombined sites on the Au surface. The prepared electrochemical sensors were rinsed several times with PBS buffer and placed in a 4 °C refrigerator for backup.

Electrochemical detection of ctDNA

The ctDNA was dispersed in TE buffer solution or diluted serum solution. To make a standard ctDNA solution, we dissolved the ctDNA powder in TE buffer. Then, 5 μL of various concentrations of standard ctDNA solution was added dropwise onto pDNA/AuNPs/Ni-CAT/CB/PPGE electrode, incubated at 37 °C for 30 min, and rinsed with the 0.01 M PBS (pH 7.4). For DPV (scanning potential of 0 ~ 0.4 V, pulse period of 0.05 s) measurement, the electrode was soaked in the 0.01 M PBS (pH 7.4) containing 0.1 M KCl and 5 mM $[Fe(CN)_6]^{3-/4-}$. In this process, the label-free detection strategy was used to assay ctDNA quickly and efficiently. The commercial healthy human serum was diluted tenfold with TE buffer and ctDNA (1 nM, 10 pM, and 0.1 pM) was spiked for serological testing. The following test procedure was used the previous one.

Results and discussion

Characterization of Ni-CAT/CB

In this study, field emission scanning electron microscopy (FE-SEM) was used to characterize the morphological structure of CB, Ni-CAT, and Ni-CAT/CB. The CB wrapped in PVA appears to be an irregular spherical shape with the diameter of about 100 nm, as shown in Fig. 1A . According to Fig. 1B , Ni-CAT is a uniform stick-like structure with a diameter of 100 nm and a length of about 1 μm. By stacking in an uneven arrangement, the nanorods formed a large number of voids, increasing the material's specific surface area. The morphology of the Ni-CAT/CB nanocomposite is shown in Fig. 1C; the CB is embedded in the voids formed by the stack of Ni-CAT nanorods, displaying a uniform microstructure with interlaced rows of nanorods and nanospheres. The Ni-CAT/CB nanocomposites were further characterized by energy dispersive spectroscopy (EDS) to identify element mapping. As displayed in Fig. 1D-G, the C, O, N, and Ni elements are homogeneously distributed in the whole materials. The results demonstrated the successful synthesis of Ni-CAT/CB and its unique morphology.

Fig. S1 shows the X-ray diffraction (XRD) patterns of CB, Ni-CAT, and Ni-CAT/CB composites, revealing the crystal structure characteristics of the above materials. As seen in Fig. S1 (curve b), multiple characteristic peaks of Ni-CAT located at $2\theta = 4.6°$, 9.3°, 14°, 16.2°, and 26.6° existed corresponding to (100), (200), (130), (201), and (002) planes, respectively [22]. In particular, the (002) plane demonstrated that the material was covalently connected as expected for a π-π laminar stacking structure. Carbon black (CB) is composed of an amorphous part and a crystalline part. The crystalline part of the CB contributed to the formation of

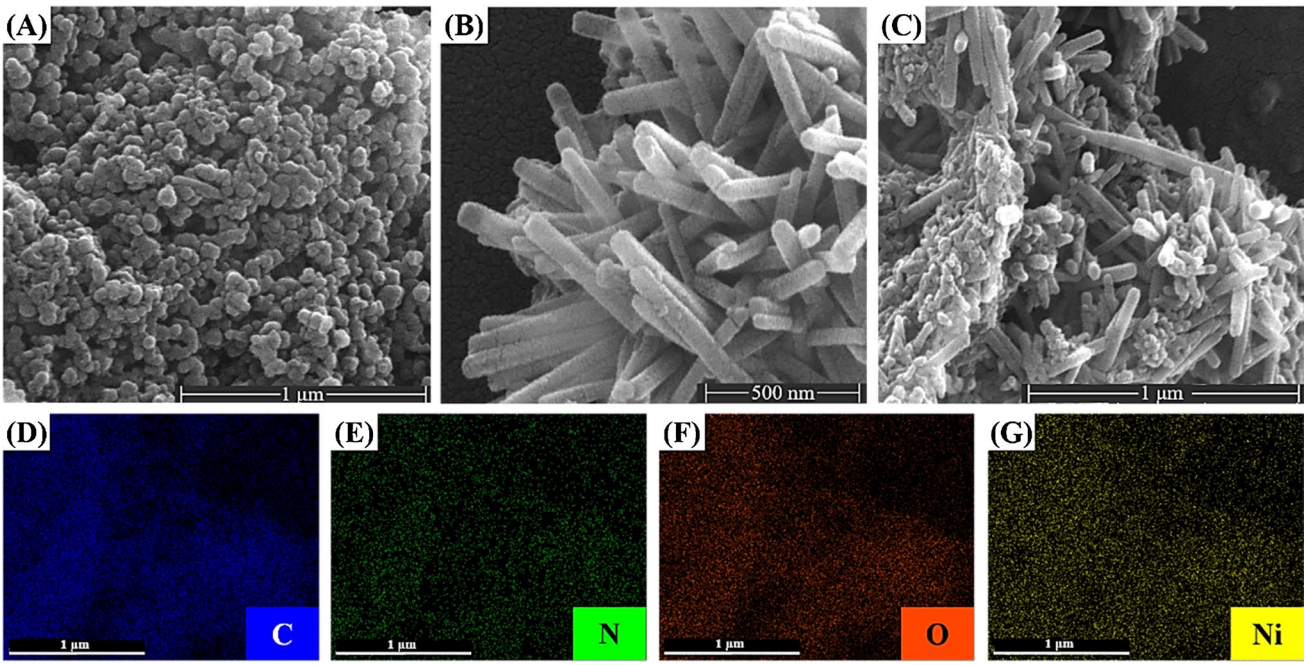

Fig. 1 SEM image of CB (**A**), Ni-CAT (**B**)E, and Ni-CAT/CB(**C**). EDS mapping of Ni-CAT/CB(D-G)

the (002) peak, while the less developed crystalline carbon and amorphous carbon affected the location and width of the (002) peak. The diffraction angle (2θ) of the 002 peak of crystalline graphite is 26.56°. In contrast, the 002 peak of CB is located near 25.1° in curve a. The position of the emergence peak moved to the left, and the peak width was larger. This result indicated that CB was mainly composed of a chaotic layer structure with incomplete stacking of carbon atom layers [23]. Meanwhile, all the characteristic peaks of curves a and b can be found in curve c. The results prove the successful preparation of the material.

The elemental composition of Ni-CAT was further analyzed by X-ray photoelectron spectroscopy, and the characteristic spin–orbit peaks of three elements, Ni 2p, O 1s, and C 1s, are demonstrated in Fig. S2. The two peaks at 856.4 eV and 861.7 eV in Fig. S2B are attributed to Ni 2p 3/2 and its satellite peaks, and similarly the two binding peaks at about 874.50 eV and 880.1 eV are attributed to Ni 2p 1/2 and its satellite peaks, respectively. These results demonstrated the presence of divalent nickel ions in Ni-CAT [24]. In Fig. S2C, the C 1s spectrum is shown, with the peak at 284.1 eV representing the C = C bond in the benzene ring. The C–O and C = O bonds are responsible for the peaks at 285.8 eV and 288.7, respectively. Fig. S2D shows the O 1s spectrum, the special peak near 531.5 eV attributed to the characteristic metal–oxygen bond (M–O), and the other peak at 533.1 eV corresponding to oxygen in the hydroxyl group (H–O) [24]. All these XPS results confirmed the formation of a conductive Ni-CAT.

Characterization of fabricated modified electrodes

Herein, the AuNPs/Ni-CAT/CB composite was used for the construction of electrochemical biosensing platform for ctDNA speedy testing. The electrocatalytic performance of the pDNA/AuNPs/Ni-CAT/ CB/PPGE was evaluated using CV measurements in PBS buffer solution (pH 7.4) containing 0.1 M KCl and 5 mM $[Fe(CN)_6]^{3-/4-}$. As shown in Fig. 2A , curves from a to e represented the redox reactions at different stages of the electrochemical sensor preparation process, as well as reflecting the conductivity and electron transfer capacity of the electrode at different stages. The curves a, b, and c correspond to the bare PGE, the PPGE, and AuNPs/Ni-CAT/CB/PPGE, respectively. After pre-treatment of PGE, the electrode surface structure has changed, forming a loose and porous structure that increased the specific surface area and facilitates electron transfer [21]. Therefore, curve b exhibited better current magnitude and reduction oxidation performance than curve a. Furthermore, Ni-CAT/CB increased the conductivity and the specific surface area of the electrode surface, and gold nanoparticles electrodeposited on the electrode surface could substantially improve the electrical conductivity. Thus, curve c showed the maximum current. Curves d and e represented the redox plots with one nucleic acid strand of pDNA added to the electrode and with two nucleic acid strands of pDNA and complementary ctDNA added, respectively. Firstly, the pDNA is bound to the sensor surface through the interaction between the sulfhydryl group and Au, resulting in a

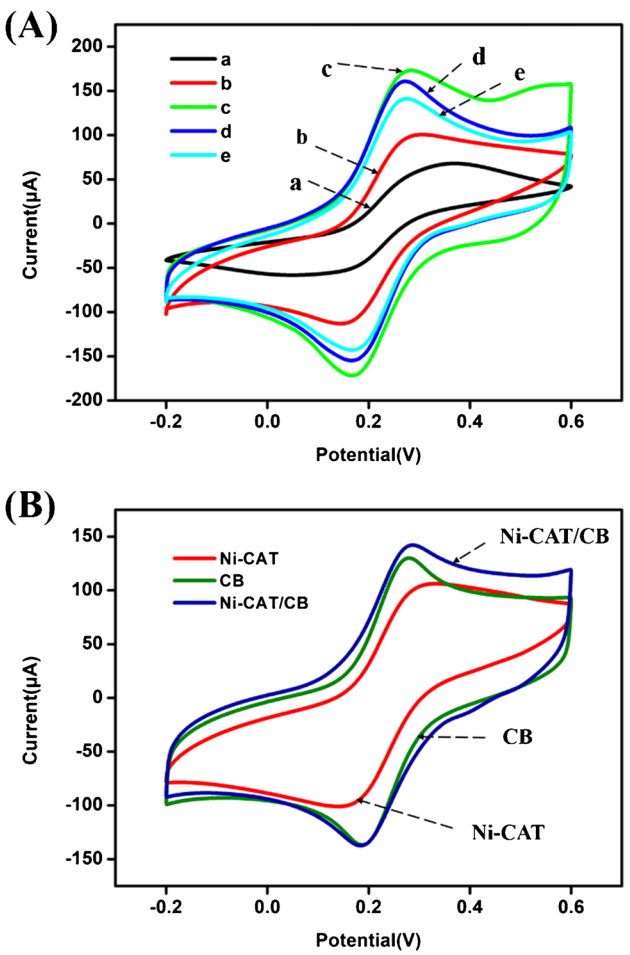

Fig. 2 CV (**A**) of bare PGE (a), PPGE (b), AuNPs/Ni-CAT/CB/PPGE (c), pDNA AuNPs/Ni-CAT/CB/PPGE (d), and ctDNA/pDNA/AuNPs/Ni-CAT/CB/PPGE (e) in PBS buffer solution (pH 7.4) containing 0.1 M KCl and 5 mM $[Fe(CN)_6]^{3-/4-}$. And CV (**B**) curves of electrodes after modification with different materials (Ni-CAT, CB, and Ni-CAT/CB)

reduction of the peak current (curve d). Then, the complementary target ctDNA interacted with the probe pDNA via the base complementary pairing, and the blocking effect caused by the DNA strands on the electrode surface caused a further reduction in current (curve e) [25].

We calculated the effective active area of different modified electrodes using CV characterization results (Fig. 2) and combined them with the Randled-Sevcik equation (Formula 1) to verify that the effective active area of the sensor gradually increased with material modification.

$$I_p = 2.69 \times 10^5 n^{\frac{3}{2}} A D^{\frac{1}{2}} \nu^{\frac{1}{2}} C \quad (1)$$

(In Formula (1), A denotes the effective surface area of this electrode (cm^2); I_p is the peak current magnitude (A) of the CV graph of this electrode; n represents the number of electrons transferred during the reductive oxidation reaction ($[Fe(CN)_6]^{3-/4-}$, $n=1$); D is the diffusion coefficient of the solution carrying out this reductive oxidation reaction, ($K_3[Fe(CN)_6]$, $(6.7 \pm 0.02) \times 10^{-6}$ cm^2/s); C is the concentration of electroactive material (5×10^{-6} mol/cm^3), and ν is the scan rate of CV (0.05 V/s).)

After calculating the effective active area of the electrode after modification with various materials, the following results were obtained in descending order: PGE (0.0872 cm^2) < PPGE (0.1293 cm^2) < Ni-CAT /PPGE (0.1364 cm^2) < CB/PPGE (0.1670 cm^2) < Ni-CAT/CB/PPGE (0.1825 cm^2) < AuNPs/Ni-CAT/CB/PPGE (0.2224 cm^2).

As shown in Fig. 2B, the conductivity of the Ni-CAT/CB composite is superior to that of Ni-CAT and CB alone. The specific surface area of the electrodes modified with the three different materials was compared to the Randled-Sevcik equation calculation. It was clear that the Ni-CAT/CB composite outperforms Ni-CAT and CB alone in terms of specific surface area. We hypothesized that the staggered arrangement of the Ni-CAT stick structure increases the number of CB attachment sites, which increases surface area and improves electron transfer to the electrode. As a result, it was clear that our choice of composite material is extremely beneficial in electrode modification.

The Nyquist spectrum in Fig. S3 led to the same conclusion. The PGE had a more extensive semicircular region. The semicircular region shrank after polarization, and the semicircular diameter of the Nyquist spectrum shrank even more after the addition of AuNPs/Ni-CAT/CB composite to the PPGE. This trend indicated that the addition of nanohybrids increased the surface's electron transfer resistance significantly, widening the gap between the electrode surface and the supporting electrolyte solution as well as the distance for charge exchange. Fig. S3B demonstrated that the attachment of DNA at the electrode can also change the size of the semicircle in the Nyquist spectrum, indicating a change in resistance at the electrode.

The comparative analysis of sensor detection principles and characterization plots of CV and EIS showed that the two trends are consistent. We also used the Randled-Sevcik equation to calculate the effective active area. All of the findings above demonstrate the success of our electrochemical sensor construction and the feasibility of target detection.

Optimization of experimental conditions

To achieve optimal sensor performance, we optimized the assay environment in the following aspects: mass ratio of Ni-CAT and CB, volume of Ni-CAT/CB added, pDNA concentration and hybridization time between pDNA and target ctDNA.

Figure 3A depicts the effect of the mass ratio of Ni-CAT to CB affected the electrochemical sensor performance. When the mass ratio of Ni-CAT and CB reached 1:2, the

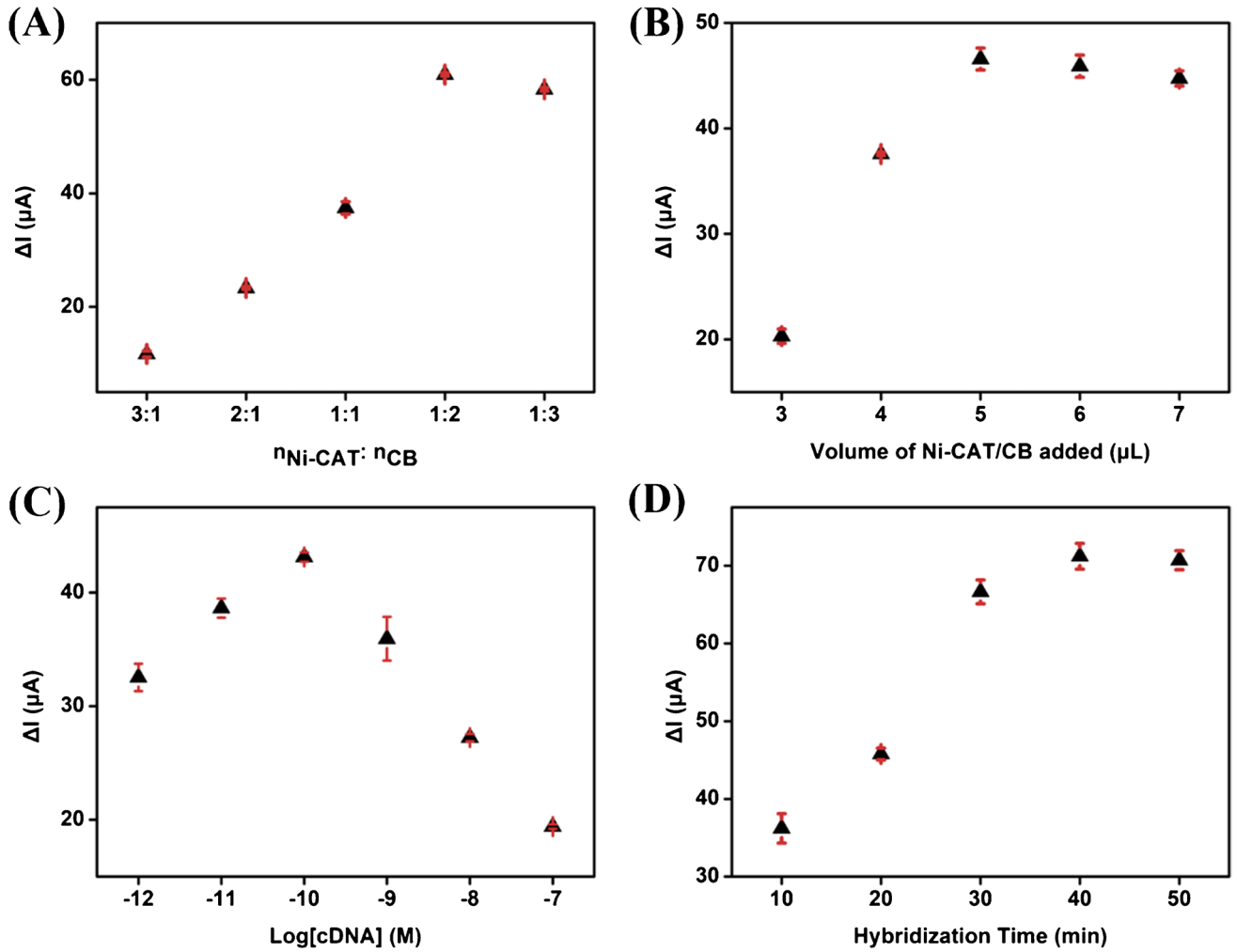

Fig. 3 Optimization of experimental conditions: the mass ratio of Ni-CAT to CB (**A**); volume of Ni-CAT/CB added (**B**); pDNA concentration (**C**); hybridization time between pDNA and target ctDNA (**D**)

nanocomposite's peak current difference (I) peaked. As demonstrated in Fig. 3B, the current steadily grew and subsequently reduced with a variety of material additions. The peak current difference (ΔI) reached the maximum when the addition amount of Ni-CAT/CB (4 mg/mL) composite is 5 μL

In addition, we looked into some pDNA-related experimental conditions. As reflected in Fig. 3C, the optimal detection results for ctDNA detection can be achieved when concentration of pDNA is 0.1 pM. Appropriate pDNA concentration ensured that there are enough active sites on the electrode and that targets with a wider concentration range can be identified more effectively. Figure 3D showed the peak difference in current (Δ*I*) as well as reaching stability when the hybridization time is up to 30 min. Thereafter, there was a slight increase in current as the hybridization time was extended. Within a reaction time of 30 min, the target forms a stable binding to the cDNA, and the rapid detection goal is achieved.

In summary, the optimal detection conditions for the experiments were as follows: the mass ratio of Ni-CAT and CB was 1:2; the volume of Ni-CAT/CB added was 5 μL; the pDNA concentration was 0.1 pM; and the optimal reaction time between pDNA and ctDNA was 30 min.

Assay performance for ctDNA detection

Different concentrations of ctDNA were assayed under optimal conditions. The prepared pDNA/AuNPs/Ni-CAT/CB/PPGE electrochemical sensors were immersed in a PBS buffer solution (pH 7.4) containing 0.1 M KCl and 5 mM $[Fe(CN)_6]^{3-/4-}$ for electrochemical studies by DPV, with the scanning voltage range from − 0.1 V to 0.5 V. After the pDNA and target were paired with each other, the ctDNA/

pDNA/AuNPs/Ni-CAT/CB/PPGE was analyzed under the same protocol. As shown in Fig. 4A, with the increasing concentration of target, the nucleic acid strand attached to the electrode surface increases, resulting in a decrease in the peak current obtained from DPV detection. Then the target was attached to the sensor surface by complementary pairing, forming a dense molecular film. This resulted in increased blocking of $[Fe(CN)_6]^{4-/3-}$ molecules at the surface of the electrode and reducing the peak current [26]. The calibration plots which showing the relative changes in the peak DPV currents for different concentrations of pDNA under optimal conditions were illustrated in Fig. 4B. In the concentration range of 1 fM to 1 μM, the calibration plots revealed a significant linear connection between the change in peak current intensity and the logarithm of target concentration. All DPV measurements were performed at least 3 times on different PPGEs. We can thus obtain the regression equation and the value of the correlation coefficient: $y = 168.333 + 10.6617 \log X$ ($R^2 = 0.99923$). Eleven blank samples were tested, and the limit of detection was calculated using the triple signal-to-noise method (3 SD/m). The calculated detection limit was 0.32 fM.

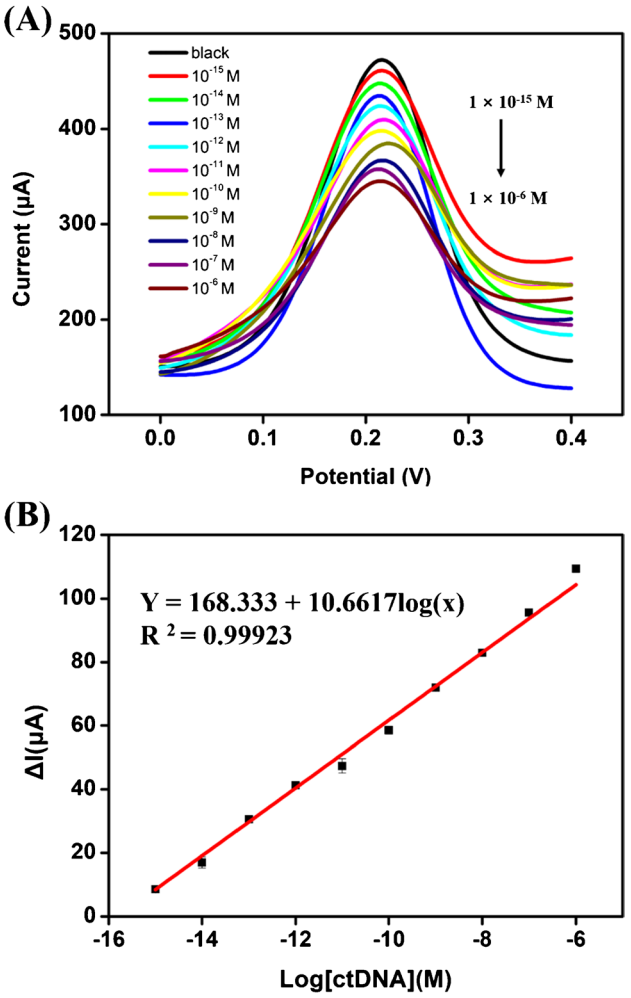

Fig. 4 (**A**) DPV (scanning potential of 0 ~ 0.4 V, pulse period of 0.05 s) response of AuNPs/Ni-CAT/CB/PPGE at various concentrations of target (1 μM–1 fM) in PBS buffer solution (pH 7.4) containing 0.1 M KCl and 5 mM $[Fe(CN)_6]^{3-/4-}$. (**B**) Calibration plot of the relative change in DPV peak current of the proposed AuNPs/Ni-CAT/CB/PPGE electrode versus the logarithm of the concentration of ctDNA

$$S = \frac{k}{A} \tag{2}$$

(In Formula (2), S is the sensitivity of sensor ($\mu A \cdot dec^{-1} \cdot cm^{-2}$); K is the slope of the linear regression equation between the logarithm of the ctDNA concentration; and ΔI ($\mu A \cdot dec^{-1}$); A is the active effective area of pDNA/AuNPs/Ni-CAT/CB/PPGE (cm^2)).

The calculated sensitivity of the pDNA/AuNPs/Ni-CAT/CB/PPGE sensor was approximately 51.584 $\mu A \cdot dec^{-1} \cdot cm^{-2}$ (Formulas (1) and (2)). The performances of the recently reported electrochemical ctDNA biosensors are listed in Table 2. In comparison, our prepared biosensor offered a detection limit and detection range that was no less than that of other methods, without complex biomagnification techniques. At the same time, the detection time of our sensor was extremely short, taking only 30 min.

Specificity, stability, and repeatability studies

There are over twenty subtypes of EGFR 19 Dels, of which, EGFR 19 del (1) and EGFR 19 del (2) account for up to 68.9%.

Table 2 Comparison of analytical characteristics of different electrochemical biosensors for detection of ctDNA

Electrode materials	Time	Amplification	Linear range	Detection limit	Ref
$NG\text{-}PEI\text{-}COF_{TAPB\text{-}TFPB}$	4.5 h	Fe-MOF for signal enhancement	100 fM–100 Nm	7.65 fM	[27]
3D graphene/AuPtPd nanoflower	140 min	CRISPR/Cas9 cleavage triggered ESDR	0.01–500 pM	0.13 pM	[28]
Gold electrode	1.5 h	Nest hybridization chain reaction	5 pM–5 nM	3 pM	[29]
DOX@TDN-Au	2 h	DNA walker and RCA	1 fM–10 nM	0.29 fM	[30]
SPGE	80 min	HAC-AuPt signal amplification label	10 nM–0.1 fM	0.036 fM	[31]
SPGE	3 h	$AuPt/3D\text{-}GHC_{600}$	10 nM–10 aM	2.25 aM	[32]
AuNPs/Ni-CAT/CB	30 min	/	1 fM–1 μM	0.32 fM	This work

Both of them change amino acids 747–750 in exon 19 [33]. So, we explored the specificity of this sensor by setting up a wild-type EGFR group, an EGFR 19 del (2) group, and a blank group to interfere with the test. As seen in the results shown in Fig. 5A, there was minimal interference in the wild-type EGFR group. Slightly more interference was seen in EGFR 19 del (2) due to greater similarity in nucleic acid sequence to the target. Overall, the interferents were all detected close to the blank group and the sensor had good specificity.

The usefulness of biosensors is greatly influenced by their stability. Therefore, the biosensor's stability was investigated. As shown in Fig. 5B , the AuNPs/Ni-CAT/CB/PPGEs are stored at 4 °C for 14 days. After 14 days, 86.48% of the sensor's current signal strength was maintained. This showed that the sensor has a high stability. In passing, we explored the stability of the same electrode modified with DNA in the $[Fe(CN)_6]^{3-/4-}$ containing solution. As seen in Fig. 5C, the RSD is 0.35% ($n = 15$) after successive DPV electrochemical assays. The pDNA/AuNPs/Ni-CAT/CB/PPGE was stable in the assay system. Furthermore, the repeatability of the sensor is investigated, as shown in Fig. 5D. All DPV electrochemical measurements were performed 5 times on different PPEGs, and the calculated RSD = 1.88% ($n = 5$). The results indicated that the sensor also had good repeatability.

Serum sample assay

We explored the practical application of this sensor for ctDNA detection in real serum samples. We selected tenfold the diluted commercial healthy human sera and sera spiked with added target ctDNA (1 nM, 10 pM, and 0.1 pM) for testing. The diluted serum also reduced the concentration of interfering substances in the serum while providing an appropriate solution environment for the DNA hybridization process. As showed in Table 3, the recoveries obtained from the assays are 93.90%, 98.83%, and 108.14%, respectively. The corresponding RSD values were 0.98%, 2.86%, and 3.95%, respectively ($n = 5$). The high level of agreement between these findings and the concentrations were provided. The relative standard deviations (RSDs) for all samples were less than 4%, indicating that our strategy was reproducible.

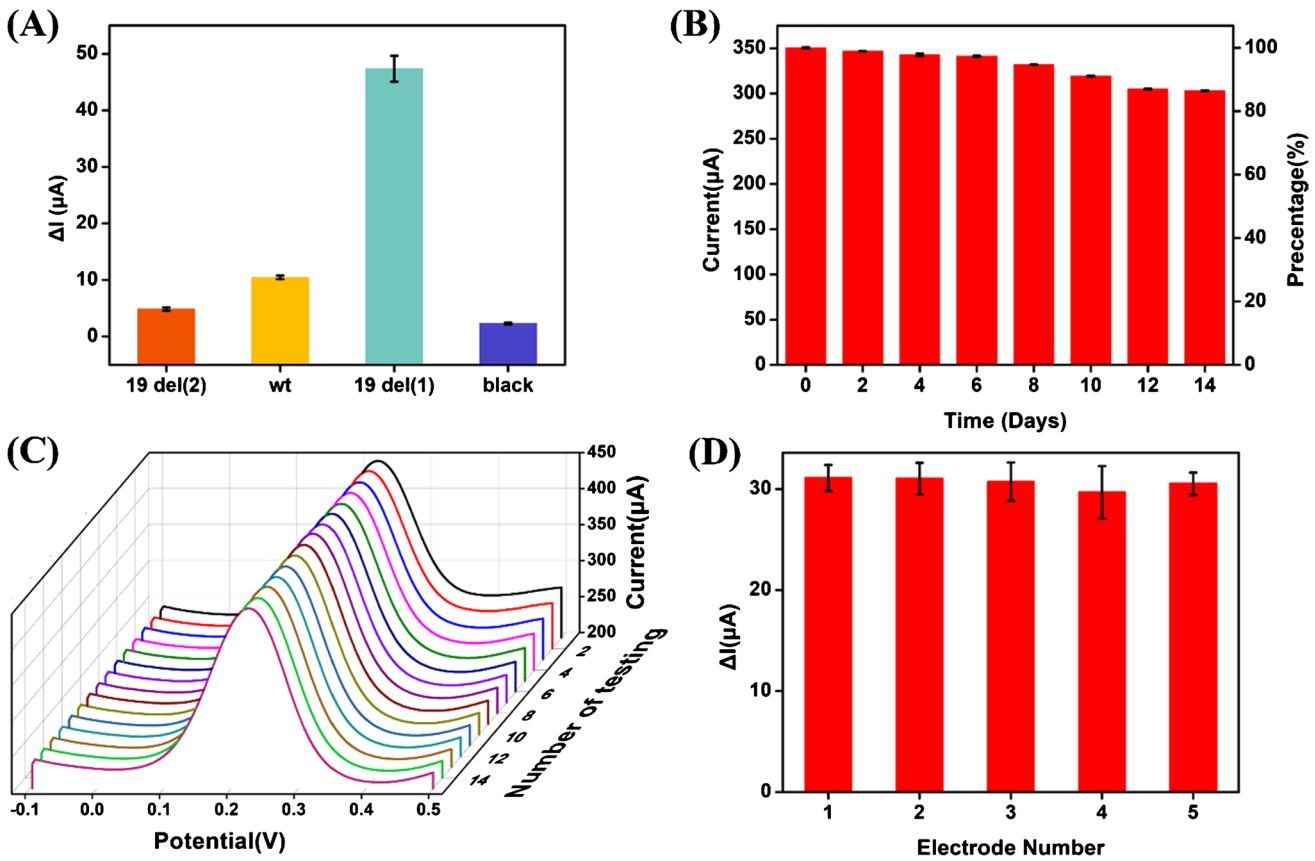

Fig. 5 (**A**) DPV response of the proposed biosensor in selectivity for ctDNA, wild-type DNA (wt), another type of mutation 19 del (2). The concentration of ctDNA was 0.1 pM, and the concentrations of the others were 1 pM. (**B**) The stability of the AuNPs/Ni-CAT/CB/PPGE storaged at 4 °C for 14 days. (**C**) Effect of PBS buffer solution (pH 7.4) containing 0.1 M KCl and 5 mM $[Fe(CN)_6]^{3-/4-}$ on pDNA/AuNPs/Ni-CAT/CB/PPGE during scanning. (**D**) The repeatability of detection on different electrodes

Table 3 Detection of ctDNA added in human serum ($N=5$) with the proposed biosensor

Sample number	Add log [ctDNA]	Detect log [ctDNA]	Recovery (%)	RSD(%) ($N=5$)
1	−9	−9.0273	93.9081%	0.98%
2	−11	−11.0051	98.8341%	2.86%
3	−13	−12.966	108.1419%	3.95%

The results indicated that the sensor has high accuracy and interference resistance to ctDNA in real samples.

Conclusions

In this work, we prepared a high-performance electrochemical biosensor by employing Ni-CAT, and CB as substrate materials, while applying a simple label-free detection procedure. Ni-CAT is a unique MOF material with high electrical conductivity. We successfully synthesized this material and investigated the benefits of its application to electrochemical sensors, as well as the possible principles. This was the first time that a conductive MOF was used in a biomacromolecule assay, taking full advantage of its admirable performance in conductivity and specific surface area. The use of label-free assay protocols made the sensing method particularly appealing for structuring point-of-care testing (POCT) devices. At the same time, the analysis process took about 30 min, which is a great advantage compared to other detection strategies. With this method, ctDNA was detected in the range of 1 f M to 1 μM and the LOD of 0.32 fM. Furthermore, the detection of ctDNA in serum also achieved satisfactory results. This work had some research implications and potential development prospects for detection of tumor markers. However, there is a long way to go in the research of portable devices, which also is a future research hot spot.

Supplementary Information The online version contains supplementary material available at https://doi.org/10.1007/s00604-022-05482-4.

Funding This work was supported by the National Natural Science Foundation of China (Nos. 81271930 and 31000425), the Research Project of Chongqing Science and Technology Commission of China (cstc2020jcyj-msxmX0861), the Fundamental Research Funds for the Central Universities (No. 2020CDJ-LHZZ-033), and we would like to thank the Analytical and Testing Center of Chongqing University for SEM images, XRD, and XPS spectrum.

Declarations

Conflict of interest The authors declare no competing interests.

References

1. Bronkhorst AJ, Ungerer V, Holdenrieder S (2019) The emerging role of cell-free DNA as a molecular marker for cancer management. Biomolecular Detection and Quantification 17:100087. https://doi.org/10.1016/j.bdq.2019.100087
2. de Lima LTF, Broszczak D, Zhang X, Bridle K, Crawford D, Punyadeera C (2020) The use of minimally invasive biomarkers for the diagnosis and prognosis of hepatocellular carcinoma. Biochimica et Biophysica Acta (BBA) Reviews on Cancer 1874(2):188451
3. Volckmar AL, Sultmann H, Riediger A, Fioretos T, Schirmacher P, Endris V et al (2018) A field guide for cancer diagnostics using cell-free DNA: from principles to practice and clinical applications. Genes Chromosom Cancer 57(3):123–139. https://doi.org/10.1002/gcc.22517
4. Newton CR, Graham A, Heptinstall LE, Powell SJ, Summers C, Kalsheker N et al (1989) Analysis of any point mutation in DNA. The amplification refractory mutation system (ARMS). Nucleic Acids Research 17(7):2503–2516
5. Mao X, Pan S, Zhou D, He X, Zhang Y (2019) Fabrication of DNAzyme-functionalized hydrogel and its application for visible detection of circulating tumor DNA. Sens Actuators, B Chem 285:385–390. https://doi.org/10.1016/j.snb.2019.01.076
6. Zhang J, Dong Y, Zhu W, Xie D, Zhao Y, Yang D et al (2019) Ultrasensitive detection of circulating tumor dna of lung cancer via an enzymatically amplified SERS-based frequency shift assay. ACS Appl Mater Interfaces 11(20):18145–18152. https://doi.org/10.1021/acsami.9b02953
7. Chaibun T, Puenpa J, Ngamdee T, Boonapatcharoen N, Athamanolap P, O'Mullane AP et al (2021) Rapid electrochemical detection of coronavirus SARS-CoV-2. Nat Commun 12(1):802. https://doi.org/10.1038/s41467-021-21121-7
8. Miao P, Tang YG (2020) DNA walking and rolling nanomachine for electrochemical detection of miRNA. Small 16(47):2004518. https://doi.org/10.1002/smll.202004518
9. Wang L-L, Chen W-Q, Wang Y-R, Zeng L-P, Chen T-T, Chen G-Y et al (2020) Numerous long single-stranded DNAs produced by dual amplification reactions for electrochemical detection of exosomal microRNAs. Biosens Bioelectron 169:112555. https://doi.org/10.1016/j.bios.2020.112555
10. Zhang R, Chen W (2015) Fe_3C-functionalized 3D nitrogen-doped carbon structures for electrochemical detection of hydrogen peroxide. Science Bulletin 60(5):522–531. https://doi.org/10.1007/s11434-015-0740-0
11. Ramachandran R, Leng X, Zhao C, Xu Z-X, Wang F (2020) 2D siloxene sheets: a novel electrochemical sensor for selective dopamine detection. Appl Mater Today 18:100477. https://doi.org/10.1016/j.apmt.2019.100477
12. Small LJ, Henkelis SE, Rademacher DX, Schindelholz ME, Krumhansl JL, Vogel DJ et al (2020) Near-zero power MOF-based sensors for NO_2 detection. Adv Func Mater 30(50):2006598. https://doi.org/10.1002/adfm.202006598
13. Song J, Huang M, Lin X, Li SFY, Jiang N, Liu Y et al (2022) Novel Fe-based metal–organic framework (MOF) modified carbon nanofiber as a highly selective and sensitive electrochemical sensor for tetracycline detection. Chem Eng J 427:130913. https://doi.org/10.1016/j.cej.2021.130913
14. Rubio-Gimenez V, Almora-Barrios N, Escorcia-Ariza G, Galbiati M, Sessolo M, Tatay S et al (2018) Origin of the chemiresistive response of ultrathin films of conductive metal-organic frameworks. Angewandte Chemie-International Edition 57(46):15086–15090. https://doi.org/10.1002/anie.201808242
15. Duan H, Zhao Z, Lu J, Hu W, Zhang Y, Li S et al (2021) When conductive MOFs meet MnO_2: high electrochemical energy

storage performance in an aqueous asymmetric supercapacitor. ACS Appl Mater Interfaces 13(28):33083–33090. https://doi.org/10.1021/acsami.1c08161
16. Cai D, Lu MJ, Li L, Cao JM, Chen D, Tu HR et al (2019) A highly conductive MOF of graphene analogue $Ni_3(HITP)_2$ as a sulfur host for high-performance lithium-sulfur batteries. Small 15(44):1902605. https://doi.org/10.1002/smll.201902605
17. Xu Z, Wang Q, Zhangsun H, Zhao S, Zhao Y, Wang L (2021) Carbon cloth-supported nanorod-like conductive Ni/Co bimetal MOF: a stable and high-performance enzyme-free electrochemical sensor for determination of glucose in serum and beverage. Food Chem 349:129202. https://doi.org/10.1016/j.foodchem.2021.129202
18. Ko M, Mendecki L, Eagleton AM, Durbin CG, Stolz RM, Meng Z et al (2020) Employing conductive metal–organic frameworks for voltammetric detection of neurochemicals. J Am Chem Soc 142(27):11717–11733. https://doi.org/10.1021/jacs.9b13402
19. Vicentini FC, Ravanini AE, Figueiredo-Filho LCS, Iniesta J, Banks CE, Fatibello-Filho O (2015) Imparting improvements in electrochemical sensors: evaluation of different carbon blacks that give rise to significant improvement in the performance of electroanalytical sensing platforms. Electrochim Acta 157:125–133. https://doi.org/10.1016/j.electacta.2014.11.204
20. Hmadeh M, Lu Z, Liu Z, Gándara F, Furukawa H, Wan S et al (2012) New porous crystals of extended metal-catecholates. Chem Mater 24(18):3511–3513. https://doi.org/10.1021/cm301194a
21. Nagarajan S, Vairamuthu R, Angamuthu R, Venkatachalam G (2019) Electrochemical fabrication of reusable pencil graphite electrodes for highly sensitive, selective and simultaneous determination of hydroquinone and catechol. J Electroanal Chem 846:113156. https://doi.org/10.1016/j.jelechem.2019.05.038
22. Nguyen NTT, Furukawa H, Gándara F, Trickett CA, Jeong HM, Cordova KE et al (2015) Three-dimensional metal-catecholate frameworks and their ultrahigh proton conductivity. J Am Chem Soc 137(49):15394–15397. https://doi.org/10.1021/jacs.5b10999
23. Lee S-M, Lee S-H, Roh J-S (2021) Analysis of activation process of carbon black based on structural parameters obtained by XRD analysis. Crystals 11(2):153 (https://www.mdpi.com/2073-4352/11/2/153)
24. Qiao Y, Liu Q, Lu S, Chen G, Gao S, Lu W et al (2020) High-performance non-enzymatic glucose detection: using a conductive Ni-MOF as an electrocatalyst. Journal of Materials Chemistry B 8(25):5411–5415. https://doi.org/10.1039/D0TB00131G
25. Tezerjani MD, Benvidi A, Jahanbani S, Moshtaghioun SM, Mazloum-Ardakani M (2016) A comparative investigation for prostate cancer detection using two electrochemical biosensors based on various nanomaterials and the linker of thioglycolic acid. J Electroanal Chem 778:23–31. https://doi.org/10.1016/j.jelechem.2016.08.009
26. Hájková A, Barek J, Vyskočil V (2017) Electrochemical DNA biosensor for detection of DNA damage induced by hydroxyl radicals. Bioelectrochemistry 116:1–9. https://doi.org/10.1016/j.bioelechem.2017.02.003
27. Guo L, Mu Z, Yan B, Wang J, Zhou J, Bai L (2022) A novel electrochemical biosensor for sensitive detection of non-small cell lung cancer ctDNA using NG-PEI-$COF_{TAPB\text{-}TFPB}$ as sensing platform and Fe-MOF for signal enhancement. Sens Actuators, B Chem 350:130874. https://doi.org/10.1016/j.snb.2021.130874
28. Chen M, Wu D, Tu S, Yang C, Chen D, Xu Y (2021) CRISPR/Cas9 cleavage triggered ESDR for circulating tumor DNA detection based on a 3D graphene/AuPtPd nanoflower biosensor. Biosens Bioelectron 173:112821. https://doi.org/10.1016/j.bios.2020.112821
29. Huang Y, Tao M, Luo S, Zhang Y, Situ B, Ye X et al (2020) A novel nest hybridization chain reaction based electrochemical assay for sensitive detection of circulating tumor DNA. Anal Chim Acta 1107:40–47. https://doi.org/10.1016/j.aca.2020.02.006
30. Li D, Xu Y, Fan L, Shen B, Ding X, Yuan R et al (2020) Target-driven rolling walker based electrochemical biosensor for ultrasensitive detection of circulating tumor DNA using doxorubicin@tetrahedron-Au tags. Biosens Bioelectron 148:111826. https://doi.org/10.1016/j.bios.2019.111826
31. Chen K, Zhao H, Wang Z, Lan M (2021) A novel signal amplification label based on AuPt alloy nanoparticles supported by high-active carbon for the electrochemical detection of circulating tumor DNA. Anal Chim Acta 1169:338628. https://doi.org/10.1016/j.aca.2021.338628
32. Chen KC, Zhao HL, Wang ZX, Lan MB (2022) Three-dimensional graphene-like homogeneous carbon architecture loaded with gold-platinum for the electrochemical detection of circulating tumor DNA. Materials Today Chemistry 24:100892. https://doi.org/10.1016/j.mtchem.2022.100892
33. Su J, Zhong WZ, Zhang XC, Huang Y, Yan HH, Yang JJ et al (2017) Molecular characteristics and clinical outcomes of EGFR exon 19 indel subtypes to EGFR TKIs in NSCLC patients. Oncotarget 8(67):111246–111257. https://doi.org/10.18632/oncotarget.22768